

Effects of mesoscale dynamics on the path of fast-sinking particles to the deep ocean: A modelling study

Lu Wang¹, Jonathan Gula^{2,3}, Jérémie Collin¹, Laurent Mémery¹

¹Univ Brest, CNRS, IRD, Ifremer, Laboratoire des Sciences de l'Environnement Marin (LEMAR), IUEM, Plouzané, France

²Univ Brest, CNRS, IRD, Ifremer, Laboratoire d'Océanographie Physique et Spatiale (LOPS), IUEM,

³Institut Universitaire de France (IUF), Paris, France

Key Points:

- The statistical funnel of deep-ocean sediment traps is mainly determined by mesoscale dynamics in the twilight zone
 - On average the vertical flow enhances particle sinking, but with more variance in spring than in other seasons
 - Coherent eddies reduce the particle dispersion within a local area, with vertical acceleration (deceleration) by anticyclones (cyclones)

Corresponding author: Lu Wang, Lu.Wang@univ-brest.fr

This article has been accepted for publication and undergone full peer review but has not been through the copyediting, typesetting, pagination and proofreading process, which may lead to differences between this version and the Version of Record. Please cite this article as doi: 10.1029/2022JC018799.

This article is protected by copyright. All rights reserved.

Abstract

The gravitational sinking of organic particles is a vital component of the biological carbon pump. This sinking process is strongly modulated by the spatiotemporally varying eddy field, complicating the interpretation of particle flux measured by deep-moored sediment traps. By backtracking particles to 200 m depth based on the outputs of a realistic eddy-resolving simulation, we characterize the origins of particles collected at a long-term observatory site in the Northeast Atlantic and focus on the impact of mesoscale dynamics on particle transport. Our results show that mesoscale dynamics between 200 m and 1000 m control the statistical funnel. Over the long term, the horizontal sampling scales of traps are estimated as hundreds of kilometers, with containment radius ranging from 90 to 490 km, depending on sinking velocities. Particle travel time suggests that overall vertical flow acts to facilitate the export, with estimated deviations up to 1 ± 2 days for particles sinking at 50 m d^{-1} to 1000 m. Statistical analyses of horizontal displacements reveal that mesoscale eddies at the site confine particle sources in a more local area. On average, particles in anticyclonic eddies sink faster to depth than expected from purely gravitational sinking, contrary to their counterparts in cyclonic eddies. The results highlight the critical role of mesoscale dynamics in determining particle transport in a typical open ocean region with moderate eddy kinetic energy. This study provides implications for the sampling design of particle flux measurements during cruises and the interpretation of deep-ocean mooring observations.

Plain Language Summary

As plants in the ocean, phytoplankton organisms transform the atmospheric CO₂ into organic carbon that forms particles of various sizes sinking to the deep ocean due to gravity. The falling particles can be collected by containers called sediment traps. However, particles may originate far from the surface ocean directly above the trap as ocean currents horizontally transport particles. Also, the time taken by particles to sink to the deep ocean varies due to vertical motions of seawater. To study the impact of ocean currents on sinking particles, we use an ocean model and virtual particles. We release particles at a fixed location, representing a sediment trap, and track particle trajectories back in time to identify their source regions. Our results show that the size of this source region is mainly determined by currents between 200-1000 m. On average, particles tend to sink faster than expected from purely gravitational sinking. Large whirlpools of water above the trap lead to a local source region, which suggests that the particle flux can be better correlated to the surface production of organic carbon in this case. The finding has implications for the sampling strategy and the interpretation of particle export measurements in regional surveys.

52 1 Introduction

53 A vital process of oceanic carbon cycling is the biological carbon pump (BCP) which
 54 sequesters atmospheric CO₂ by exporting photosynthetically-produced organic carbon from
 55 the surface layer to the deep ocean (Falkowski et al., 1998). The BCP is mainly regulated
 56 by the sinking particulate organic carbon (POC) produced in the euphotic zone (Riley et
 57 al., 2012; Sanders et al., 2014; Henson et al., 2015; Turner, 2015). Long-term observations
 58 of the downward particle flux are available from moored sediment traps over recent decades
 59 (Lampitt & Antia, 1997; Buesseler et al., 2007; Lampitt et al., 2010; Le Moigne et al.,
 60 2013). Traditionally, POC export through gravitational sinking is evaluated from a quasi-
 61 one-dimensional (1D) viewpoint, which couples particle interception by sediment traps with
 62 particle production in the surface ocean directly above the trap (Deuser & Ross, 1980; Asper
 63 et al., 1992; Armstrong et al., 2001). However, particles are also affected by horizontal
 64 advection during their vertical sinking (Siegel et al., 1990; Deuser et al., 1990; Burd et al.,
 65 2010). Consequently, impacts of hydrodynamics on sinking particles challenge the link of
 66 particle collection at depth with surface signatures (Dever et al., 2021), and hence promote
 67 the extrapolation of POC export in a spatiotemporally varying circulation field.

68 The concept of the statistical funnel has been raised to construct a dynamical source
 69 region enclosing the likely origins of particles settling to time-series sediment traps (Siegel &
 70 Deuser, 1997). The statistical funnel is often characterized by analyzing Lagrangian particles
 71 backtracked from the trap location to the surface ocean. Waniek et al. (2000) identified ori-
 72 gins of particles from separated, distant regions by daily-mean observed current profiles at a
 73 quasi time-series station in the northeast Atlantic. Siegel et al. (2008) constructed statistical
 74 funnels for a deep-moored trap in the Pacific ocean using a combination of satellite-derived
 75 geostrophic velocities and shipboard ADCP profiles. They estimated horizontal scales larger
 76 than 300 km for a trap at 4000 m collecting particles sinking at 50 m d⁻¹. Such a sampling
 77 scale is confirmed by Qiu et al. (2014) with the use of a time-dependent 3D velocity field
 78 of a circulation model. Furthermore, studies of Liu et al. (2018) and Wekerle et al. (2018)
 79 both showed that the statistical funnels vary with the trap location and seasons, and high-
 80 lighted the presence of eddies in determining the particle sources. These studies have shown
 81 that the statistical funnel of moored sediment traps depends on trap depth, particle sinking
 82 velocity, collection time, and regional advective processes.

83 Ocean mesoscale dynamics exert influences on POC export by generating a heteroge-
 84 neous distribution of primary production that produce sinking particles (Mahadevan, 2016;
 85 Lvy et al., 2018), and by directly modulating particle transport (Boyd et al., 2019). Mecha-
 86 nisms of the physical-biological interactions at mesoscale have been demonstrated in terms
 87 of eddy stirring, trapping, and pumping (Olson, 1991; McWilliams, 2008; McGillicuddy,
 88 2016). Eddies can horizontally advect and diffuse particles (Deuser et al., 1988; Siegel et
 89 al., 1990, 2008), and add an additional advective vertical flux of POC in the eddy-related
 90 frontal region (Stukel et al., 2017). Also, eddies can structure the subsurface distribution of
 91 particles, leading to a deep-reaching funnel of particles towards the eddy center (Waite et al.,
 92 2016). Furthermore, mesoscale dynamics may have an impact on the POC export at smaller
 93 scales (Klein & Lapeyre, 2009). In the horizontal, strong surface convergent zones associ-
 94 ated with submesoscale cyclonic fronts are found to concentrate materials into tight clusters
 95 within a short time (Poje et al., 2014; McGillicuddy, 2016; DAsaro et al., 2018), leading
 96 to a preferred accumulation of buoyant material into mesoscale cyclones (Vic et al., 2022).
 97 While in the vertical, large vertical velocities generated at submesoscale frontal structures
 98 extend from the surface down to hundreds of meters (Mahadevan & Tandon, 2006; Klein &
 99 Lapeyre, 2009; Lvy et al., 2012). The magnitude of vertical velocity in different dynamical
 100 regimes ranges from $\mathcal{O}(10)$ m d⁻¹ to $\mathcal{O}(100)$ m d⁻¹ (Pietri et al., 2021), comparable to the
 101 majority of particle sinking velocities accounting for carbon fluxes at depth (50-200 m d⁻¹)
 102 (Turner, 2002). The control of vertical flows on the travel time of particles is important for
 103 sediment trap measurements, especially during the period of rapid spring blooms (Asper et
 104 al., 1992). In this manner, the local vertical velocity field may considerably affect particle

105 export from the upper ocean. Observations have shown elevated POC flux generated by
 106 the stretching features in the frontal region between mesoscale eddies (Guidi et al., 2012).
 107 The elevations were mostly detected within the mixed layer, though the mixed layer base
 108 did not appear to obstruct the particle export. Intensified mesoscale eddies may also pro-
 109 duce deep-reaching submesoscale fronts that penetrate well below the mixed layer (Yu et
 110 al., 2019; Siegelman et al., 2020). Such findings suggest enormous potential impacts of
 111 mesoscale eddies and their associated submesoscale dynamics on the fate of particle export
 112 to the deep ocean.

113 As an interface between the well-studied epipelagic layer (sunlight zone) and the dark
 114 deep ocean, the mesopelagic layer (also known as the “twilight zone”) spanning from 200
 115 m to 1000 m is a crucial element in the rapid removal of carbon further down to the deep
 116 ocean. However, the understanding of the role of the twilight zone in carbon transport
 117 remains to be improved from physical, biogeochemical, and ecological perspectives (Martin
 118 et al., 2020). Since 2019, the Joint Exploration of the Twilight Zone Ocean Network (JET-
 119 ZON) has been set up to provide a new scientific understanding of the twilight zone. It
 120 coordinates a variety of international projects, one of which is the French project APERO
 121 (Assessing marine biogenic matter Production, Export and Remineralization from the sur-
 122 face to the dark Ocean), built on an upcoming intensive field program at the Porcupine
 123 Abyssal Plain sustained observatory (PAP-SO) in the open-ocean region of Northeast At-
 124 lantic. The PAP site allows simultaneous studies of both upper ocean and abyssal depths,
 125 where deep-sea POC flux has been measured over decades using a long-term sediment trap
 126 mooring. Scheduled for June 2023 when the export peaks, the cruise of APERO follows
 127 the US EXPORTS cruise to the same location during the bloom/post-bloom period in May
 128 (Siegel et al., 2016).

129 Motivated by the sustained observations and upcoming APERO cruise in the PAP
 130 region, this study aims to identify the source region of particles collected by deep-ocean sed-
 131 iment traps, and investigate how mesoscale patterns shape the statistical funnel of particles.
 132 We use outputs from an eddy-resolving regional ocean model to backtrack particles from the
 133 PAP site. The findings will have implications for the design of the Process Study Stations
 134 to be deployed during the APERO cruise. This work assesses for the first time the impact
 135 of small/medium-scale dynamics on the dispersion of sinking particles in the mesopelagic
 136 layer (200–1000 m), once exported below the surface mixed layer. The paper is organized as
 137 follows. Section 2 provides information on the ocean circulation simulations and Lagrangian
 138 experiment design. Section 3 presents results of particle backtracking, including statistical
 139 funnels, horizontal and vertical dispersion, and the role of specific flow structures on particle
 140 transport. Finally, we offer conclusions and discussion on the findings in Section 4.

141 2 Experiment Setup

142 The particle backtracking experiments are designed to reconstruct a large number of
 143 particle trajectories from sediment trap locations to the upper boundary of the twilight zone.
 144 Our goals are to characterize statistical funnels of deep-ocean sediment trap sampling, and
 145 to relate their spatio-temporal variability to underlying mesoscale dynamics.

146 2.1 Numerical model outputs

147 Instantaneous outputs at 12 hourly intervals from a realistic eddy-resolving model are
 148 used to compute particle trajectories. The simulation was performed using CROCO (Coastal
 149 and Regional Ocean COmmunity model) built upon ROMS (Shchepetkin & McWilliams,
 150 2005) which solves the hydrostatic primitive equations for the momentum and state vari-
 151 ables. The configuration (POLGYR) has 2000×1600 grid points covering the North At-
 152 lantic Subpolar Gyre. The horizontal grid spacing is 2 km, much smaller than the first
 153 Rossby deformation radius over this domain (10–20 km) (Chelton et al., 1998). There are
 154 80 vertical sigma levels, with a variable resolution following the topography (about 5 m

155 at the surface and 40 m at the bottom, up to 100 m for the maximum vertical spacing in
 156 the intermediate layer). After a two-year spin-up time, the simulation is run from 2001 to
 157 2009, and we use the seven years between 2002 and 2008. The use of 12-hourly wind forcing
 158 and the absence of tides largely reduces the generation of internal waves and high-frequency
 159 variability.

160 Le Corre et al. (2020) provide a detailed description of the simulation, and validation
 161 through comparisons of the mean circulation as well as mesoscale activity, with observations
 162 from drifters and Argo floats. In this study, we focus on the southeastern portion of the
 163 whole domain, with a size of 1600×1600 km centered on the PAP site (49°N , 16.5°W).
 164 The study region is characterized by moderate kinetic energy compared to the western and
 165 northern parts of the subpolar gyre (Figure 1a). The mean flow in this region is around
 166 0.05 m s^{-1} (Le Cann, 2005); such a weak advection enables particles initially seeded at
 167 the PAP site to stay within this subdomain for several months. The circulation in this
 168 region is dominated by mesoscale eddy activity. A stream of cyclonic and anticyclonic
 169 eddies intermittently crosses the PAP site (Figure 1b), feeding the site with an eastward
 170 meandering North Atlantic Current branch, and flows from the European shelf (Hartman
 171 et al., 2010).

172 2.2 Lagrangian particle tracking

173 We use a Python/Fortran hybrid parallelized code, named “Pyticles” (Gula & Collin,
 174 2021), to track offline particles backward to their source locations. Particles evolve in the
 175 native Arakawa C-grid and terrain-following vertical coordinates of the ocean model. The
 176 model fields are linearly interpolated at particle positions in space and time. The numerical
 177 time scheme for advection is Runge-Kutta 4, with a time step of 2 minutes, which ensures
 178 that the Courant-Friedrichs-Lowy condition is satisfied. The Lagrangian model has a good
 179 performance in the reversibility of particle tracking, with errors of $\mathcal{O}(10^{-4})$ m for horizontal
 180 displacement and $\mathcal{O}(10^{-7})$ m for vertical displacement, over a travel distance of $\mathcal{O}(10)$
 181 km. Sensitivity tests verified that increasing the frequency of CROCO snapshots used for
 182 experiments from 12h to 1h, or using averages instead of snapshots, has a negligible impact
 183 on the statistical results of particle dispersion (Figure S1) and vertical velocities (Figure S2).
 184 Therefore, 12h instantaneous outputs are sufficient to capture particle dynamics for such a
 185 typical open-ocean region where mesoscale currents dominate, and sources of high-frequency
 186 variability such as submesoscale currents and internal waves are not fully resolved.

187 A series of experiments is performed to backtrack particles monthly collected over the
 188 seven years (2002–2008). The seeding depths are chosen at 1000 m and 2000 m, representing
 189 the bottom of the twilight zone and a standard depth of the deep-ocean sediment traps,
 190 respectively. This study focuses on the impact of mesoscale dynamics in the mesopelagic
 191 layer once particles are exported below the mixed layer. Hence the base of the epipelagic
 192 layer, 200 m, is chosen as the end depth where source locations of particles are determined.
 193 This depth is also a typical depth of the deep winter mixed layer in this region (Yu et al.,
 194 2019; Coatanoan, 2021). Four constant sinking speeds (200, 100, 50, and 20 m d⁻¹) are
 195 assigned to particles. They are mostly endorsed by observations at the PAP site giving the
 196 range of particle sinking rates from 30 m d⁻¹ (Villa-Alfageme et al., 2014) to 180 m d⁻¹
 197 (Riley et al., 2012). Particles are initialized every 12 hours within a 10×10 km seeding
 198 patch centered on the PAP site, corresponding to 6×6 grid points with one particle located
 199 at each grid point. The choice of the patch size implicitly considers the dispersion due to
 200 subgrid-scale mixing, as there is no parameterized diffusivity in the Lagrangian model. We
 201 have tested that the exact location of the particles inside the patch does not impact our
 202 results by performing additional experiments with particles randomly seeded in the patch
 203 (not shown). In each experiment, particles are injected continuously every 12 h over one
 204 month and are tracked until they reach 200 m. The total number of particles for a monthly
 205 analysis is 2160 (i.e. 36×60).

206 To investigate how the dynamical regimes of horizontal advection change with depth,
 207 we also deploy depth-keeping particles on the horizontal plane at different depths. The
 208 seeding patch and the timing of particle release in these 2D experiments are the same as in
 209 the 3D ones.

210 3 Results

211 3.1 Statistical funnel of deep-ocean sediment traps

212 3.1.1 Overview of the source regions

213 The distribution of particle source regions at 200 m shows a synoptic picture of the
 214 sampling area resulting from the integrated horizontal advection over time and space (Figure
 215 2). Mesoscale eddies transport particles from distant regions to the PAP site, which forms a
 216 diffuse cloud of particle sources at the export depth. Such an effect has been indicated in Vic
 217 et al. (2018) by comparing the dispersion pattern driven by mesoscale currents to that by the
 218 mean flow. The sensitivity experiments here indicate that the catchment area of a moored
 219 sediment trap increases with the trap depth (top panel vs. bottom panel) and decreases
 220 with particle sinking velocity (e.g., from (a) to (d) on the top panel). Qualitatively, changes
 221 in the sampling area with sinking velocity are more significant than changes due to the trap
 222 depth. The area with particle density exceeding $10^{-2}\%$ for 2000 m trap remains almost
 223 the same as for the 1000 m trap, whereas the radius of this area reduces by hundreds of
 224 kilometers when particle sinking velocity increases from 20 m d^{-1} to 200 m d^{-1} . It suggests
 225 that the dynamics between 1000 m and 2000 m does not effectively alter the statistical
 226 funnel as much as that in the twilight zone (200-1000 m).

227 The source regions are further quantified using a set of basic metrics (Table 1). Mean
 228 displacements (r_{mean}) range from 47 km to 190 km for the collection at 1000 m, with only
 229 a modest increase of < 50 km for the collection at 2000 m. The collection scale of deep-
 230 moored sediment traps is as large as 100 km, even for fast-sinking particles. Containment
 231 radii ($R_{95\%}$), defined as the radial distance covering 95% of a source region, are 90 and
 232 118 km for particles sinking velocity of 200 m d^{-1} . The $R_{95\%}$ dramatically increases as the
 233 sinking velocity decreases, with the largest value of 490 km for particles sinking at 20 m d^{-1}
 234 to the trap at 2000 m. Our estimates of the mean displacement and containment radii are
 235 much larger than the estimates obtained by Siegel et al. (2008) due to the higher-resolution
 236 velocity field and the larger subsurface EKE in our study region. The percentage of area
 237 with probability densities larger than $10^{-2}\%$ confirms that changes of source area with
 238 sinking velocity are more significant than with trap depths.

239 Figure 3 shows the vertical structure of statistical funnels by integrating trajectories of
 240 particles from 2000 m projected on the zonal section. The funnels of particles sinking at
 241 100 m d^{-1} and 200 m d^{-1} have limited widths with less variability over depth. By contrast,
 242 the collection of the two slower sinking classes is primarily controlled by the dynamics
 243 changing with depth, especially the twilight zone, as indicated by the widened bounds. The
 244 broadening of funnels between 200 m and 1000 m coincides with vertical profiles of eddy
 245 kinetic energy (EKE) and root-mean-square vertical velocity w_{rms} (Figure 3e-f). The former
 246 indicates horizontal transport, while the latter influences the shape of statistical funnels by
 247 affecting the sinking time of particles. The magnitude of EKE and w_{rms} are comparable to
 248 the OSMOSIS mooring observations (Yu et al., 2019). EKE shows a rapid decay from over
 249 $100 \text{ cm}^2 \text{ s}^{-2}$ in the upper ocean, down to $20 \text{ cm}^2 \text{ s}^{-2}$ at 1000 m, and remains at such low level
 250 from here. The vertical velocity w_{rms} is intensified up to 40 m d^{-1} at 200 m during winter
 251 months when submesoscale motions are active, and at around 20 m d^{-1} for autumn and
 252 summer when mesoscale activity dominates. The slight linear increase of w_{rms} with depth
 253 below 1000 m corresponds to a bottom intensification of vertical flows due to interactions
 254 with topography. As such, the influence of vertical flows is considerable for the 20 and 50 m
 d^{-1} particle groups. Based on the two profiles, the water column below the epipelagic layer

can be divided into three layers with different regimes: Energetic layer (200-500 m) with high EKE and large w_{rms} , Active layer (500-1000 m) with still relatively high but decaying EKE and small w_{rms} , Quiescent layer (> 1000 m) with weak and relatively steady flows (Figure 3g).

3.1.2 Statistics of the source regions

A source region of particles is taken as a particle cloud for statistical analysis. We adopt the general notions in LaCasce (2008) to quantify the variability of particle source regions. Three moments (mean, variance, and kurtosis) are derived from the probability density function (PDF) of the horizontal displacements for monthly backtracking of particles.

The mean describes the movement of the center of mass

$$M = \sqrt{M_x^2 + M_y^2} \quad (1)$$

with

$$M_x = \frac{1}{N} \sum_{i=1}^N [x_i - x_{i_0}], \quad (2)$$

$$M_y = \frac{1}{N} \sum_{i=1}^N [y_i - y_{i_0}], \quad (3)$$

where (x_i, y_i) gives the horizontal position of particle i when it reaches 200 m depth, and (x_{i_0}, y_{i_0}) is its initial position.

The horizontal displacement relative to the center of mass for a single particle is given by

$$r_i = \sqrt{[x_i - x_{i_0} - M_x]^2 + [y_i - y_{i_0} - M_y]^2}. \quad (4)$$

The variance measures how particles spread out, namely, the size of the particle cloud (also referred to as "cloud dispersion")

$$\begin{aligned} D &= \frac{1}{N-1} \sum_{i=1}^N ([x_i - x_{i_0} - M_x]^2 + [y_i - y_{i_0} - M_y]^2) \\ &= \frac{1}{N-1} \sum_{i=1}^N r_i^2. \end{aligned} \quad (5)$$

The kurtosis is used to reflect the spatial distribution of particles

$$ku \equiv \frac{\sum_i r_i^4}{[\sum_i r_i^2]^2}. \quad (6)$$

A kurtosis close to 3 corresponds to a PDF following a nearly Gaussian distribution, which is the case for randomly moving particles. In contrast, particles advected by turbulent flows tend to distribute in tight clusters, characterized by a kurtosis higher than 3.

We choose particles sinking at 50 m d^{-1} backtracked from 1000 m as an example for the following analyses. This choice is a good compromise between the realistic range of sinking velocity and the ability to reflect the influence of flow dynamics in the twilight zone. The 20 m d^{-1} sinking group is shown in the time series as well to indicate how slow-sinking particles are affected.

The center of mass mostly moves around the PAP site within a diameter of 100 km for particles sinking at 50 m d^{-1} and 200 km for the sinking group 20 m d^{-1} (Figure 4a), as

shown by the source areas in Figure 2. The two sinking groups show similar variability in the monthly statistical funnel: local kurtosis peaks appear to arise with low mean and variance. Since the end of 2002, valleys of variance often occur with small means and large kurtosis, corresponding to a local source region with a center of mass adjacent to the PAP site. Kurtosis peaks larger than 3 indicate extended tails in the PDF of horizontal displacement, which means the distribution of particles is highly heterogeneous (Figure 4c).

The presence of mesoscale eddies is most likely responsible for shaping particle distributions. Three indicators depict local mesoscale activity within a 100 km × 100 km area centered on the PAP site (Figure 4d-f). Sea level anomaly (SLA) reveals eddy features at the surface, relative vorticity $\zeta = v_x - u_y$ and Okubo-Weiss parameter $OW = \sigma^2 - \zeta^2$ where the strain magnitude $\sigma = \sqrt{(u_x - v_y)^2 + (v_x + u_y)^2}$, indicate signatures of mesoscale eddies at 500 m. We highlight eight periods based on their dispersion metrics showing local peaks of kurtosis with low mean and variance, associated with distinct signals of mesoscale eddies (half anticyclones and half cyclones, marked by the blue/red vertical lines in Figure 4). A reference period, January 2006, is chosen to compare with the former periods. Note that the reference period is characterized by a higher variance, much lower kurtosis, and no signature of local mesoscale dynamics.

3.2 Horizontal advection

3.2.1 Horizontal dispersion in the 3D field

Source distributions of particles collected at 1000 m during two representative eddy-dominated periods and the reference period are shown in the top panel of Figure 5. Particle sources were highly concentrated around the PAP site during December 2002 and May 2007, in response to the local presence of mesoscale eddies (Figure 5d and f). In contrast, no particular hot-spot of particle source locations is seen embracing the PAP site in January 2006 when the vorticity does not dominate (Figure 5e). This situation is representative of conditions without a single-dominant eddy structure.

The measures in Figure 4 derived from the PDF of horizontal displacements have described the shape of statistical funnels as a result of particle dispersion. We adopt notions in Poje et al. (2010) to further describe the temporal evolution of horizontal dispersion by computing single-particle dispersion and pair dispersion (Figure 5g-h). The former, also termed absolute dispersion, describes the spreading of particles. Denoting the trajectory of a particle by $\mathbf{x}(\mathbf{a}, t)$ where the label $\mathbf{a} = \mathbf{x}(\mathbf{a}, t_0)$, the horizontal absolute dispersion A_h^2 is defined as the mean-squared horizontal displacement

$$A_h^2(t) = \langle (\mathbf{x}_h(\mathbf{a}, t) - \mathbf{a}_h)^2 \rangle \quad (7)$$

where $\langle \rangle$ denotes the ensemble average. The horizontal relative dispersion D_h^2 measures particle pair dispersion that depicts the stirring process. That is, the mean-squared horizontal separation of particle pairs initially defined at the beginning of particle release. The relative separation of a particle pair $(\mathbf{a}_1, \mathbf{a}_2)$ is computed as

$$\mathbf{D}(t, \mathbf{D}_0) = \mathbf{D}_0 + (\mathbf{x}(\mathbf{a}_1, t) - \mathbf{x}(\mathbf{a}_2, t)) \quad (8)$$

with the initial distance between the two particles in a pair $\mathbf{D}_0 = \mathbf{a}_1 - \mathbf{a}_2$. Here we consider the horizontal separation only:

$$D_h^2(t) = \langle \mathbf{D}_h(t) \cdot \mathbf{D}_h(t) \rangle \quad (9)$$

The horizontal absolute dispersion A_h^2 first follows a ballistic regime $A_h^2(t) \propto t^2$ at small time scales of several days. The non-locality indicates the dominance of mesoscale dynamics in absolute dispersion. At intermediate time scales, an anomalous dispersion regime occurs with $A_h^2(t) \propto t^\alpha$ where α varies between 1 and 2. A diffusive regime $A_h^2(t) \propto t$

337 characterized by a slope close to 1 is expected after a long time when the absolute dispersion
 338 linearly grows in time. However, the large spatio-temporal inhomogeneities in mesoscale
 339 ocean flow often prevent the presence of such a regime. The slopes for December 2002 and
 340 May 2007 ultimately fall below 1 as most particles stay trapped within an eddy and cannot
 341 spread further.

342 Relative dispersion depicts smaller-scale motions affecting relative diffusivity. It shows
 343 less difference in slopes. The horizontal relative dispersion D_h^2 first shows an exponential
 344 growth within approximately 5 days, typically occurring at spatial scales smaller than the
 345 deformation radius (10-20 km). In the next stage, D_h^2 follows a regime $D^2(t) \propto t^\beta$ with
 346 $2 < \beta < 3$ related to motions at local scales. The evolution of absolute and relative dispersion
 347 suggests reduced particle spread when a strong eddy persists around the PAP site.

348 3.2.2 Dynamical regimes of horizontal dispersion

349 Horizontal dispersion in the 3D field is also affected by vertical dispersion. Particles
 350 of the same age can vertically separate by a few hundred meters when backtracked into
 351 the upper ocean. Particles may thus experience different dynamical regimes over a range
 352 of depths and may also be affected by a vertical shear (Berti & Lapeyre, 2021). Results of
 353 2D experiments illustrate different dynamical regimes from 200 m down to 4000 m. The
 354 visual appearance of particle trajectories suggests the dominance of mesoscale activity in
 355 transporting and trapping particles (Figure 6a-c). Comparisons between trajectories at
 356 different depths identify that the transition depths for dynamical regimes are 500 m and
 357 1000 m, consistent with the three-layer structure of the water column in Figure 3. In the
 358 energetic regime of horizontal advection above 500 m, particles from 200 km away or further
 359 can also reach the site in the reference case (January 2006). At the base of the twilight zone
 360 (1000 m), the regime switches from the upper ocean with active eddies to the quiescent deep
 361 ocean. The clusters of dispersion curve for the upper ocean, middle, and deeper depths verify
 362 the regimes categorized by 2D trajectories. At intermediate stage (about 5 days), the power-
 363 law regime $D^2(t) \propto t^\beta$ with $2 < \beta < 3$ is only seen at depths above 1000 m. It underlines
 364 the existence of small-scale motions in the upper two layers. Similar to 3D experiments, the
 365 flattening dispersion curves starting from about 5 days after the release for December 2002
 366 and May 2007 illustrate lower dispersion of particles in the twilight zone, mostly confined
 367 within the 200×200 km box.

368 3.3 Vertical advection

369 To evaluate the impact of vertical advection, we examine the time taken by particles
 370 to sink from the export depth to the trap depth, termed as “travel time”. The influence of
 371 vertical flow on particle sinking can be reflected by the travel time anomaly Δt , which is the
 372 difference between the travel time t and the standard sinking time t_0 without the presence of
 373 ocean vertical flows. The amplitude of the monthly mean Δt for particles backtracked from
 374 1000 m can reach up to 7% (~ 1 day) of the expected travel time for 50 m d^{-1} particles
 375 and 12% (~ 5 days) for 20 m d^{-1} (Figure 7a-b). For individual particles, the maximal
 376 amplitude can reach up to 5 days for 50 m d^{-1} particles and 20 days for 20 m d^{-1} . Such
 377 time lags are significant for POC measurements during bloom/post-bloom periods when
 378 the production rapidly varies over days. On average, the negative $\Delta t/t_0$ in most of the
 379 experiments indicates that particles take less time to reach the trap due to the acceleration
 380 by downward ocean vertical velocity. There is no distinct seasonality found in mean Δt .
 381 However, the variance $V(\Delta t)$ commonly peaks in spring, in agreement with large vertical
 382 velocities between 200 - 400 m during this period (Figure 3e-f). The standard deviation
 383 reaches up to 2 days for 50 m d^{-1} particles and 6 days for 20 m d^{-1} . In Figure 7c, the
 384 distribution of seasonal and full-period Δt for particles sinking at 50 m d^{-1} shows a broader
 385 PDF in spring, in line with the seasonal variability of $V(\Delta t)$. The PDF of travel time t
 386 for the full period also displays slight asymmetry towards shorter time, and the asymmetry
 387 is more distinct for smaller sinking velocities and deeper trap depth (Figure 7d-e). Liu et

388 al. (2018) found that the vertical advection in the upper 200 m largely intensifies particle
 389 export with sinking speeds from 20 to 100 m d⁻¹. Our results additionally show that the
 390 vertical advection below 200 m also enhances the export of particles.

391 3.4 Linking the particle export with specific features

392 Following the work of Balwada et al. (2021), we use the joint probability distribution
 393 function (JPDF) of vorticity and strain to decompose the flow field into regions with differ-
 394 ent dynamical features. The term “vorticity” refers to the vertical component of vorticity
 395 normalized by the Coriolis frequency ζ/f , where $\zeta = v_x - u_y$. The “strain” is the strain
 396 magnitude normalized by the Coriolis frequency σ/f , where $\sigma = \sqrt{(u_x - v_y)^2 + (v_x + u_y)^2}$.
 397 The JPDF identifies three regions in the flow field separated by the lines of $\sigma = |\zeta|$: anti-
 398 cyclonic vorticity dominated (AVD) region where $\zeta < 0$ and $\sigma < |\zeta|$; cyclonic vorticity
 399 dominated (CVD) region where $\zeta > 0$ and $\sigma < |\zeta|$; and strain dominated (SD) region where
 400 $\sigma > |\zeta|$. Figure 8 shows the JPDF of full-period Lagrangian data and Eulerian field for the
 401 two layers of the twilight zone (200–500 m and 500–1000 m). The Lagrangian JPDF on the
 402 top row of Figure 8 displays no distinct skewness. Hence, particles do not show a specific
 403 preference in sampling different flow structures over the long term.

404 Vertical velocity patterns are qualitatively similar between the Eulerian and Lagrangian
 405 diagnostics. At all depths, the AVD region is featured with downwelling, whereas the CVD
 406 region is dominated by upwelling, in accord with the picture of the vertical velocity below
 407 the mixed layer in Balwada et al. (2021). In the SD region, vertical velocity patterns
 408 change with depth. Below 500 m, vertical velocities are negative close to the line $\sigma = \zeta$,
 409 corresponding to the cyclonic side of fronts, and positive on the anticyclonic side (Figure
 410 8h). Such a pattern is expected from frontal dynamics, and again in accord with results
 411 shown in Balwada et al. (2021) below the mixed-layer. However, between 200 m and 500 m,
 412 only upwelling is visible in the SD region on both sides, apparently contradicting classical
 413 expectations.

414 An important difference in our computation is that the vorticity and strain are com-
 415 puted at the same depth as the vertical velocity, which is different from the vorticity-strain
 416 space defined at the surface only in Balwada et al. (2021). Comparisons between the w
 417 patterns depending on the depth chosen to compute vorticity and strain are shown in Figure
 418 S3. If the vorticity and strain are computed at the surface, we recover the expected signs
 419 for vertical velocity: downwelling on the cyclonic side and upwelling on the other side at
 420 all depths (100 m, 200 m, 500 m). However, when the vorticity and strain are computed
 421 at the corresponding depth of vertical velocity, the patterns are reversed at 200 m and 500
 422 m. This can be attributed to the presence of numerous frontal structures with an inversion
 423 of sign for relative vorticity in the vertical, while the sign of vertical velocity remains verti-
 424 cally homogeneous (Figure S4). This is a robust feature in our simulation for all times and
 425 locations, and it will be addressed further in future research.

426 Patterns of particles and their associated vertical velocities are shown more specifically
 427 for cases corresponding to the presence of anticyclonic or cyclonic eddies in Figure 9. On the
 428 top row, the composite distribution of particles on the vorticity-strain space for months with
 429 coherent anticyclonic eddies shows a high density of particles along the $\sigma = -\zeta$ line, with a
 430 preference in the SD region (Figure 9a). These particles are likely located in the filamentary
 431 vorticity streaks along with the swirl, which highlights the footprints of particles on the
 432 periphery of the eddy. Vertical velocities recorded by particles in Figure 9b also show
 433 upward velocities despite the dominance of downward velocities, consistent with the full-
 434 period pattern in Figure 8b and d. From the PDF of travel time anomaly Δt , we find
 435 that the upward velocities are mostly associated with March 2007, which has a longer tail
 436 towards positive Δt and slight skewness. It differs from the other three months in winter
 437 and summer with apparently skewed PDF towards negative Δt , as more energetic eddies in
 438 spring allow particles to sample complex flow structures. Therefore, even the same type of

439 mesoscale features can exert different impacts on the vertical dispersion of particles. Unlike
 440 the strain-dominated pattern in the anticyclone case, particle trajectories in cyclonic eddies
 441 concentrate in the CVD region with only a smaller portion in the SD part (Figure 9d). The
 442 cyclonic vortex is responsible for the majority of upward velocities recorded by particles,
 443 leading to a PDF of Δt significantly extended to the positive side, especially in spring
 444 months.

445 Overall, JPDFs show major trends here: at monthly time scales, anticyclonic eddies
 446 accelerate the downward transport while cyclonic eddies delay the descent of particles. How-
 447 ever, the patchy vertical velocity patterns in mesoscale eddies are more complicated than
 448 the classic eddy-pumping mechanism that upwelling is always in cyclonic eddies and down-
 449 welling is always in anticyclonic eddies. This mechanism is more applicable in the period of
 450 formation and strengthening of eddies, whereas the case of eddy decay shows opposite pat-
 451 terns (Klein & Lapeyre, 2009). Furthermore, the vertical velocity patterns in eddies are not
 452 in general uniform. Instead, a set of upward and downward cells are formed extending from
 453 the center to the perimeter (Pilo et al., 2018). Besides, many other mechanisms including
 454 eddy propagation (McGillicuddy et al., 1995), eddy-eddy interactions (Pidcock et al., 2013)
 455 and submesoscale processes (Brannigan, 2016) may also contribute to the vertical velocity
 456 structure within the eddy. The complexity of mechanisms implies that a detailed analysis
 457 of individual eddies (e.g., eddy age and status, particle location) is required to link particle
 458 export with specific features.

4 Discussion and Conclusions

460 In this study, we backtracked virtual particles from locations of deep-moored sediment
 461 traps to the export depth using a realistic eddy-resolving simulation. We applied a set
 462 of dispersion metrics to characterize particle trajectories and link them with mesoscale
 463 dynamical features. Here we summarise the main conclusions and discuss the simplifications
 464 in our work and implications for future study.

4.1 On the simplifications

4.1.1 Export depth

467 We found that mesoscale dynamics in the twilight zone (200-1000 m) play a dominant
 468 role in shaping the statistical funnels based on several simplifications. We choose the base
 469 of the epipelagic layer (200 m) as the end depth of particle backtracking. The reason is
 470 that we are focusing on the fate of particles once they are formed and exported below the
 471 productive surface layer. However, the uniform end depth in our study is not precisely
 472 an export depth. The export depth, in reality, varies with time and space and differs for
 473 particles with different sinking velocities.

4.1.2 Particle sinking velocity

474 Another simplification is that we use constant sinking velocities ranging between 20
 475 and 200 m d⁻¹. Most of our choices fall into the common range of sinking velocities from
 476 50 to 200 m d⁻¹ adopted in previous studies (Siegel & Deuser, 1997; Waniek et al., 2000;
 477 Siegel et al., 2008). It is noteworthy that 20 m d⁻¹ has also been used in a few recent studies
 478 of sediment trap catchment area (Liu et al., 2018; Wekerle et al., 2018). However, particle
 479 sinking velocity is highly likely to vary with depth. Remineralization leads to a decrease
 480 in the size of particles and possibly in their sinking velocity. Dever et al. (2021) suggests
 481 remineralization processes promote the contribution of slow-sinking particles (0.025-5 m
 482 day⁻¹) to the POC export. For the fast-sinking particles in our study, we assume the
 483 impact of remineralization is modest due to the short travel time. This consideration is
 484 supported by observations at the PAP site that demonstrate that fast-sinking particles were

486 sufficient to supply deep POC flux. In contrast, slow-sinking particles were likely to be
 487 entirely remineralized in the twilight zone (Riley et al., 2012).

488 Furthermore, processes including aggregation, fragmentation, and zooplankton grazing
 489 also change particle size, density, and hence sinking velocity during particle descent (Boyd
 490 & Trull, 2007; Guidi et al., 2007; Trull et al., 2008; Riley et al., 2012). Considering the
 491 sinking velocity varying with depth, the statistical funnel of particles reaching the trap will
 492 be a mixture of source regions for a wide range of sinking classes. Nevertheless, this study
 493 deals with the impact of mesoscale dynamics on the dispersion and travel time of particles
 494 assumed to be conservative in the mesopelagic layer. Future research is required to include
 495 processes behind the changes in particle size and sinking rate (which are beyond the scope
 496 of this study).

497 4.1.3 The heterogeneity of particle sources

498 This study analyzes statistical funnels sampled by deep sediment traps without consider-
 499 ing the heterogeneity of particle sources. We identify the distribution of potential particle
 500 sources but do not address the temporal and spatial variability of carbon fluxes at depth.
 501 Both satellite observations (Zhang et al., 2019) and modeling investigations (Lvy et al.,
 502 2014) have shown undoubtedly that the dynamics at medium and small scales strongly con-
 503 trol the intensity of the primary production. The intensity of primary production largely
 504 constrains particle size spectra: higher production is generally associated with larger sizes
 505 (Kostadinov et al., 2009). Although simple relationships between particle size and sinking
 506 velocity are not straightforward (Iversen & Lampitt, 2020), to a first approximation, these
 507 two parameters can be related by Stokes' law (Lerman A., 1974; LaurenceauCorneec et al.,
 508 2020). Therefore, the next step will be to examine the impact of sinking velocity variability
 509 by weighting the particle size distribution correlated with the PP intensity at the time and
 510 location of particle formation. The primary production distributions could be estimated by
 511 coupling the dynamic model with a simple NPZD model. From a model perspective, this
 512 exercise will give us the first information on the eddy-scale variability of carbon fluxes in
 513 the deep ocean with a daily resolution. Also, it will allow a first analysis of the (de)coupling
 514 between export production below the mixed layer and deep fluxes at mesoscales (with nev-
 515 ertheless, the conservation of particles as a strong hypothesis at the first stage). In addition,
 516 by using "realistic" simulations from operational models, these backward simulations can
 517 provide relevant information about sources and time lags of particles collected in sediment
 518 traps during process study cruises.

519 4.2 Implications for studying the POC flux

520 4.2.1 Submesoscale motions below the mixed layer

521 From a physical perspective, the end depth of 200 m is close to the typical deep winter
 522 mixed layer depth in our study region. As such, submesoscale processes, which are more
 523 intense within the winter mixed layer, appear to play a minor role in particle transport below
 524 200 m. Previous studies have found that submesoscale dynamics can enhance particle export
 525 through advecting slow-sinking particles (Dever et al., 2021) or restratifying the mixed layer
 526 to reduce the impact of vertical mixing on gravitational settling (Taylor et al., 2020). The
 527 rapid accumulation of particles has also been observed in the surface convergence zones
 528 associated with large vertical velocities (Poje et al., 2014; DAsaro et al., 2018), such areas
 529 also have the potential to be hot spots of particle export to the deep ocean. However, how
 530 much submesoscale motions come into play below the mixed layer remains unclear.

531 Although highlighting the importance of mesoscale dynamics, this study points to an
 532 emergence of submesoscale motions below the mixed layer. There is a skewness in the
 533 vorticity-strain JPDF of the Eulerian field, extending along $\sigma = \zeta$ towards the cyclonic side
 534 of the frontal region. In addition, the asymmetry in the travel time anomaly reflects a skewed

535 distribution of w towards downward velocity. The two findings unveil the manifestation of
 536 submesoscale motions characterized by positive skewness of relative vorticity (Rudnick, 2001;
 537 Buckingham et al., 2016) and an enhancement of downwelling (Thomas et al., 2008; Dever
 538 et al., 2021). Thus, higher resolution modeling is in demand to disentangle the impact of
 539 smaller scales in the mesopelagic layer, which may not be negligible. Yet we should keep
 540 in mind that the influence of submesoscale motions to export in this region is limited due
 541 to the constricted overlap of strong submesoscale instabilities in winter and large particle
 542 export in spring and summer (Erickson & Thompson, 2018).

543 *4.2.2 The sampling design of a regional survey*

544 This study underlines the impact of mesoscale dynamics in the twilight zone on the 3D
 545 transport of particles at a temperate open-ocean site. The presence of coherent mesoscale
 546 eddies can effectively “trap” particles within a local area (<100 km) over a monthly time
 547 scale. Given the smaller statistical funnel confined by eddies, the export flux measured by
 548 the deep-ocean sediment traps is easier to be correlated to the surface production when
 549 a coherent structure persists right above the trap. This finding has implications for the
 550 sampling design in a regional survey, for example, the cruise scheduled in 2023 for the
 551 APERO project. As is often done during field surveys, the location of process study stations
 552 can be identified by focusing on these coherent mesoscale patterns, highlighted by satellite
 553 observations and modeling outputs. However, these structures only cover about 20% of the
 554 ocean, and particles are not always completely moving with these eddies. The eight eddy-
 555 dominated months in our analysis are based on the PDF of horizontal particle displacements.
 556 In general, high kurtosis correspond to low variance, associated with a negative Okubo-Weiss
 557 parameter and high relative vorticity (Figure 10). It indicates that coherent structures lead
 558 to hot spots of particle sources. Nevertheless, the continuum between coherent structures
 559 and turbulent flows (high variance, small kurtosis close to 3) represents a large portion of
 560 the ocean and should also be sampled. Thus sampling the remaining more turbulent and
 561 chaotic ocean is fundamental and challenging.

562 *4.2.3 Generalization to other regions*

563 While we expect our results to qualitatively hold in other regions of the ocean, the size of
 564 the statistical funnel and amplitude of the travel time anomalies will be a function of the local
 565 hydrodynamical properties, in particular of the mesoscale turbulence. A first attempt to
 566 generalize our results can be made by casting them in terms of non-dimensional parameters.
 567 We use the containment radii ($R_{95\%}$) and normalized root-mean-square travel time anomaly
 568 ($\Delta t_{RMS}/t_0$) to describe horizontal and vertical dispersion of particles, respectively, and relate
 569 them with the ratio of particle sinking velocity to the flow velocity (Figure 11). The size
 570 of particle source regions for the trap at 1000 m has $R_{95\%}$ mainly in the range of 300-400
 571 km for w_{sed}/U_{RMS} at 0.001. It decreases by half when w_{sed}/U_{RMS} increases to 0.003. For
 572 a much higher speed ratio like 0.007 and 0.014, the containment radii remain at around
 573 100 km or less. The vertical dispersion is most significant when w_{sed}/w_{RMS} is 1, with the
 574 percentage of travel time anomaly close to 15% (~ 5 days). The deviation matters for the
 575 short-term deployment of sediment traps during the bloom/post-bloom period. Note that
 576 the relationship between dispersion metrics and speed ratio depends on the trap depth. For
 577 the trap at 2000 m, the source region expands only by a few tens of kilometers compared to
 578 1000 m. The travel time anomaly increases more obviously. The 75th percentile for 20 m
 579 day⁻¹ is more than 15%, which is equivalent to 15 days. Even for 50 m day⁻¹, it is around
 580 10% (4 days). If such relationships hold for other dynamical regimes, these numbers could
 581 be a reference for estimating the source region and time lags of particle sinking, given by
 582 the current velocity data at other locations.

583 Moreover, we proposed a three-layer structure of dynamical regimes, as reflected by
 584 flow properties and horizontal dispersion in 2D experiments. In particular, the PAP site is
 585 characterized by a moderate mesoscale activity compared to other regions like the Gulf of

Mexico (Liu et al., 2018) and the Arctic ocean (Wekerle et al., 2018). The vertical structuring of particle dispersion associated with small-scale dynamics (200-500 m: high EKE and w, 500 - 1000 m: still relatively high EKE, but small w; below 1000 m: quiet, smooth flows) must be confronted with different situations. It is necessary to verify the generalization of this finding in other regions. Future work could be first at a regional scale to check the homogeneity of dispersion statistics in the inter gyre region of the North Atlantic, near the PAP station. Secondly, a similar analysis could be conducted at other long-term observatory stations (e.g., BATS, HOT) and *in situ* experiments in Eastern Boundary Upwelling Systems, where many dedicated cruises have been conducted. Lastly, different turbulent and dynamical regimes such as Western Boundary Currents and the Southern Ocean, where the correlation between strong turbulent regimes and horizontal velocities remains a big issue, are also hotspots worth studying.

Open Research

CROCO ocean model is available at <https://www.croco-ocean.org>. The Lagrangian particle tracking software Pyticles is available at <https://github.com/Mesharou/Pyticles> and has been published on Zenodo at <https://doi.org/10.5281/zenodo.4973786>.

Acknowledgments

This work was supported by the ISblue project, an Interdisciplinary graduate school for the blue planet (ANR-17-EURE-0015), and co-funded by a grant from the French government under the program "Investissements d'Avenir". This manuscript contributes to the APERO project funded by the National Research Agency under the grant APERO [grant number ANR ANR-21-CE01-0027] and by the French LEFE-Cyber program. Simulations were performed using HPC resources from GENCI-TGCC (grant 2018-A0050107638) and from DATARMOR of "Pôle de Calcul Intensif pour la Mer" at Ifremer, Brest, France. The authors thank Mathieu Le Corre for providing CROCO simulation outputs. We appreciate the three reviewers for their constructive comments and insightful suggestions that significantly helped improve this manuscript.

613 References

- 614 Armstrong, R., Lee, C., Hedges, J., Honjo, S., & Wakeham, S. (2001). A new, mechanistic
 615 model for organic carbon fluxes in the ocean based on the quantitative association of
 616 POC with ballast minerals. *Deep Sea Research Part II: Topical Studies in Oceanog-
 617 raphy*, 49(1-3), 219–236.
- 618 Asper, V., Deuser, W., Knauer, G., & Lohrenz, S. (1992). Rapid coupling of sinking particle
 619 fluxes between surface and deep ocean waters. *Nature*, 357, 670–672.
- 620 Balwada, D., Xiao, Q., Smith, S., Abernathey, R., & Gray, A. (2021). Vertical fluxes
 621 conditioned on vorticity and strain reveal submesoscale ventilation. *Journal of Physical
 622 Oceanography*, 51(9), 2883–2901.
- 623 Berti, S., & Lapeyre, G. (2021). Lagrangian pair dispersion in upper-ocean turbulence in
 624 the presence of mixed-layer instabilities. *Physics of Fluids*, 33(3), 036603.
- 625 Boyd, P., Claustre, H., Levy, M., Siegel, D., & Weber, T. (2019). Multi-faceted particle
 626 pumps drive carbon sequestration in the ocean. *Nature*, 568(7752), 327–335.
- 627 Boyd, P., & Trull, T. (2007). Understanding the export of biogenic particles in oceanic
 628 waters: Is there consensus? *Progress in Oceanography*, 72(4), 276–312.
- 629 Brannigan, L. (2016). Intense submesoscale upwelling in anticyclonic eddies. *Geophysical
 630 Research Letters*, 43(7), 3360–3369.
- 631 Buckingham, C., Naveira Garabato, A., Thompson, A., Brannigan, L., Lazar, A., Marshall,
 632 D., ... Belcher, S. (2016). Seasonality of submesoscale flows in the ocean surface
 633 boundary layer. *Geophysical Research Letters*, 43(5), 2118–2126.
- 634 Buesseler, K., Lamborg, C., Boyd, P., Lam, P., Trull, T., Bidigare, R., ... Wilson, S.
 635 (2007). Revisiting carbon flux through the ocean's twilight zone. *Science*, 316(5824),
 636 567–570.
- 637 Burd, A., Hansell, D., Steinberg, D., Anderson, T., Arstegui, J., Baltar, F., ... Tanaka,
 638 T. (2010). Assessing the apparent imbalance between geochemical and biochemical
 639 indicators of meso- and bathypelagic biological activity: What the @\\$! is wrong with
 640 present calculations of carbon budgets? *Deep Sea Research Part II: Topical Studies
 641 in Oceanography*, 57(16), 1557–1571.
- 642 Chelton, D., Deszoeke, R., Schlax, M., Naggar, K., & Siwertz, N. (1998). Geographical
 643 variability of the first baroclinic rossby radius of deformation. *Journal of Physical
 644 Oceanography*, 28, 28.
- 645 Coatanoan, C. (2021). *Mixed layer depth in the north atlantic ocean. product information
 646 document (pidoc)*. <https://doi.org/10.13155/79588>.
- 647 Deuser, W., Muller-Karger, F., Evans, R., Brown, O., Esaias, W., & Feldman, G. (1990).
 648 Surface-ocean color and deep-ocean carbon flux: how close a connection? *Deep Sea
 649 Research Part A. Oceanographic Research Papers*, 37(8), 1331–1343.
- 650 Deuser, W., Muller-Karger, F., & Hemleben, C. (1988). Temporal variations of particle
 651 fluxes in the deep subtropical and tropical north atlantic: Eulerian versus lagrangian
 652 effects. *Journal of Geophysical Research*, 93, 6857.
- 653 Deuser, W., & Ross, E. (1980). Seasonal change in the flux of organic carbon to the deep
 654 sargasso sea. *Nature*, 283, 364–365.
- 655 Dever, M., Nicholson, D., Omand, M., & Mahadevan, A. (2021). Sizedifferentiated export
 656 flux in different dynamical regimes in the ocean. *Global Biogeochemical Cycles*, 35(3).
- 657 DAsaro, E., Shcherbina, A., Klymak, J., Molemaker, J., Novelli, G., Guigand, C., ... zgk-
 658 men, T. (2018). Ocean convergence and the dispersion of flotsam. *Proceedings of the
 659 National Academy of Sciences*, 115(6), 1162–1167.
- 660 Erickson, Z., & Thompson, A. (2018). The seasonality of physically driven export at
 661 submesoscales in the northeast atlantic ocean. *Global Biogeochemical Cycles*.
- 662 Falkowski, P., Barber, R., & Smetacek, V. (1998). Biogeochemical controls and feedbacks
 663 on ocean primary production. *Science*, 281(5374), 200–206.
- 664 Guidi, L., Calil, P., Duhamel, S., Bjrkman, K., Doney, S., Jackson, G., ... Karl, D. (2012).
 665 Does eddy-eddy interaction control surface phytoplankton distribution and carbon
 666 export in the north pacific subtropical gyre? *Journal of Geophysical Research: Bio-
 667 geosciences*, 117(G2).

- 668 Guidi, L., Stemmann, L., Legendre, L., Picheral, M., Prieur, L., & Gorsky, G. (2007).
 669 Vertical distribution of aggregates (.110 mm) and mesoscale activity in the northeast-
 670 ern atlantic: Effects on the deep vertical export of surface carbon. *Limnology and*
 671 *Oceanography*, 52(1), 7–18.
- 672 Gula, J., & Collin, J. (2021). *Pyticles: a Python/Fortran hybrid parallelized code for 3D*
 673 *Lagrangian particles advection using ROMS/CROCO model data*. Zenodo. Retrieved
 674 from <https://doi.org/10.5281/zenodo.4973786> doi: 10.5281/zenodo.4973786
- 675 Hartman, S., Larkin, K., Lampitt, R., Lankhorst, M., & Hydes, D. (2010). Seasonal
 676 and inter-annual biogeochemical variations in the porcupine abyssal plain 20032005
 677 associated with winter mixing and surface circulation. *Deep Sea Research Part II:*
 678 *Topical Studies in Oceanography*, 57, 1303–1312.
- 679 Henson, S., Yool, A., & Sanders, R. (2015). Variability in efficiency of particulate organic
 680 carbon export: A model study: Variability in export ratio. *Global Biogeochemical*
 681 *Cycles*, 29(1), 33–45.
- 682 Iversen, M., & Lampitt, R. (2020). Size does not matter after all: No evidence for a
 683 size-sinking relationship for marine snow. *Progress in Oceanography*, 189, 102445.
- 684 Klein, P., & Lapeyre, G. (2009). The oceanic vertical pump induced by mesoscale and
 685 submesoscale turbulence. *Annual Review of Marine Science*, 1(1), 351–375.
- 686 Kostadinov, T., Siegel, D., & Maritorena, S. (2009). Retrieval of the particle size distribution
 687 from satellite ocean color observations. *Journal of Geophysical Research*, 114(C9),
 688 C09015.
- 689 LaCasce, J. (2008). Statistics from lagrangian observations. *Progress in Oceanography*,
 690 77(1), 1-29.
- 691 Lampitt, R., & Antia, A. (1997). Particle flux in deep seas: regional characteristics and
 692 temporal variability. *Deep Sea Research Part I: Oceanographic Research Papers*, 44(8),
 693 1377-1403.
- 694 Lampitt, R., Salter, I., de Cuevas, B., Hartman, S., Larkin, K., & Pebody, C. (2010). Long-
 695 term variability of downward particle flux in the deep northeast atlantic: Causes and
 696 trends. *Deep Sea Research Part II: Topical Studies in Oceanography*, 57(15), 1346-
 697 1361.
- 698 LaurenceauCornec, E., Le Moigne, F. C., Gallinari, B., M.and Moriceau, Toulec, J., Iversen,
 699 M., Engel, A., & De La Rocha, C. (2020). New guidelines for the application of stokes'
 700 models to the sinking velocity of marine aggregates. *Limnology and Oceanography*,
 701 65(6), 1264-1285.
- 702 Le Cann, B. (2005). Observed mean and mesoscale upper ocean circulation in the midlati-
 703 tude northeast atlantic. *Journal of Geophysical Research*, 110(C7), C07S05.
- 704 Le Corre, M., Gula, J., & Trguier, A.-M. (2020). Barotropic vorticity balance of the north
 705 atlantic subpolar gyre in an eddy-resolving model. *Ocean Science*, 16(2), 451-468.
- 706 Le Moigne, F. A. C., Henson, S. A., Sanders, R. J., & Madsen, E. (2013). Global database
 707 of surface ocean particulate organic carbon export fluxes diagnosed from the 234th
 708 technique. *Earth System Science Data*, 5, 295-304.
- 709 Lerman A., D. M., Lal D. (1974). Stokes settling and chemical reactivity of suspended
 710 particles in natural waters. In G. R.J. (Ed.), *Suspended solids in water*. (Vol. 4).
 711 Boston, MA.: Springer.
- 712 Liu, G., Bracco, A., & Passow, U. (2018). The influence of mesoscale and submesoscale
 713 circulation on sinkingparticles in the northern gulf of mexico. *Elemenata: Science of the*
 714 *Anthropocene*, 6(1), 36.
- 715 Lvy, M., Ferrari, R., Franks, P., Martin, A., & Rivire, P. (2012). Bringing physics to life at
 716 the submesoscale. *Geophysical Research Letters*, 39(14), L14602.
- 717 Lvy, M., Franks, P., & Smith, K. (2018). The role of submesoscale currents in structuring
 718 marine ecosystems. *Nature Communications*, 9(1), 4758.
- 719 Lvy, M., Jahn, O., Dutkiewicz, S., & Follows, M. (2014). Phytoplankton diversity and
 720 community structure affected by oceanic dispersal and mesoscale turbulence: Dispersal
 721 impact on plankton diversity. *Limnology and Oceanography: Fluids and Environments*,
 722 4(1), 67-84.

- Mahadevan, A. (2016). The impact of submesoscale physics on primary productivity of plankton. *Annual Review of Marine Science*, 8(1), 161-184.
- Mahadevan, A., & Tandon, A. (2006). An analysis of mechanisms for submesoscale vertical motion at ocean fronts. *Ocean Modelling*, 14(3-4), 241-256.
- Martin, A., Boyd, P., Buesseler, K., Cetinic, I., Claustre, H., Giering, S., ... Guidi, L. (2020). Study the twilight zone before it is too late. *Nature*, 580, 26-28.
- McGillicuddy, D. (2016). Mechanisms of physical-biological-biogeochemical interaction at the oceanic mesoscale. *Annual Review of Marine Science*, 8(1), 125-159.
- McGillicuddy, D., Robinson, A., & McCarthy, J. (1995). Coupled physical and biological modelling of the spring bloom in the north atlantic (ii): three dimensional bloom and post-bloom processes. *Deep Sea Research Part I: Oceanographic Research Papers*(8), 1359-1398.
- McWilliams, J. (2008). The nature and consequences of oceanic eddies. In M. Hecht & H. Hasumi (Eds.), *Geophysical monograph series* (Vol. 177, p. 5-15). Washington, D. C.: American Geophysical Union.
- Olson, D. (1991). Rings in the Ocean. *Annual Review of Earth Planet Science*, 19, 283-311.
- Pidcock, R., Martin, A., Allen, J., Painter, S., & Smed, D. (2013). The spatial variability of vertical velocity in an iceland basin eddy dipole. *Deep Sea Research Part I: Oceanographic Research Papers*, 72, 121-140.
- Pietri, A., Capet, X., dOvidio, F., Levy, M., Le Sommer, J., Molines, J.-M., & Giordani, H. (2021). Skills and limitations of the adiabatic omega equation: How effective is it to retrieve oceanic vertical circulation at mesoscale and submesoscale? *Journal of Physical Oceanography*, 51(3), 931-954.
- Pilo, G., Oke, P., Coleman, R., Rykova, T., & Ridgway, K. (2018). Patterns of vertical velocity induced by eddy distortion in an ocean model: Vertical velocity and eddy distortion. *Journal of Geophysical Research: Oceans*(3), 2274-2292.
- Poje, A., Haza, A., zgkmen, T., Magaldi, M., & Garraffo, Z. (2010). Resolution dependent relative dispersion statistics in a hierarchy of ocean models. *Ocean Modelling*, 31(1-2), 36-50.
- Poje, A., Ozgokmen, T., Lipphardt, B., Haus, B., Ryan, E., Haza, A., ... Mariano, A. (2014). Submesoscale dispersion in the vicinity of the deepwater horizon spill. *Proceedings of the National Academy of Sciences*, 111(35), 12693-12698.
- Qiu, Z., Doglioli, A., & Carlotti, F. (2014). Using a lagrangian model to estimate source regions of particles in sediment traps. *Science China Earth Sciences*, 57, 2447-2456.
- Riley, J., Sanders, R., Marsay, C., Le Moigne, F., Achterberg, E., & Poulton, A. (2012). The relative contribution of fast and slow sinking particles to ocean carbon export: Export of fast and slow sinking poc. *Global Biogeochemical Cycles*, 26(1).
- Rudnick, D. L. (2001). On the skewness of vorticity in the upper ocean. *Geophysical Research Letters*, 28(10), 2045-2048.
- Sanders, R., Henson, S., Koski, M., De La Rocha, C., Painter, S., Poulton, A., ... Martin, A. (2014). The biological carbon pump in the north atlantic. *Progress in Oceanography*, 129, 200-218.
- Shchepetkin, A., & McWilliams, J. (2005). The regional oceanic modeling system (roms): a split-explicit, free-surface, topography-following-coordinate oceanic model. *Ocean Modelling*, 9(4), 347-404.
- Siegel, D., Buesseler, K., Behrenfeld, M., Benitez-Nelson, C., Boss, E., Brzezinski, M., ... Steinberg, D. (2016). Prediction of the export and fate of global ocean net primary production: The exports science plan. *Frontiers in Marine Science*, 3.
- Siegel, D., & Deuser, W. (1997). Trajectories of sinking particles in the sargasso sea: modeling of statistical funnels above deep-ocean sediment traps. *Deep Sea Research Part I: Oceanographic Research Papers*, 44, 1519-1541.
- Siegel, D., Fields, E., & Buesseler, K. (2008). A bottom-up view of the biological pump: Modeling source funnels above ocean sediment traps. *Deep Sea Research Part I: Oceanographic Research Papers*, 55(1), 108-127.
- Siegel, D., Granata, T., Michaels, A., & Dickey, T. (1990). Mesoscale eddy diffusion,

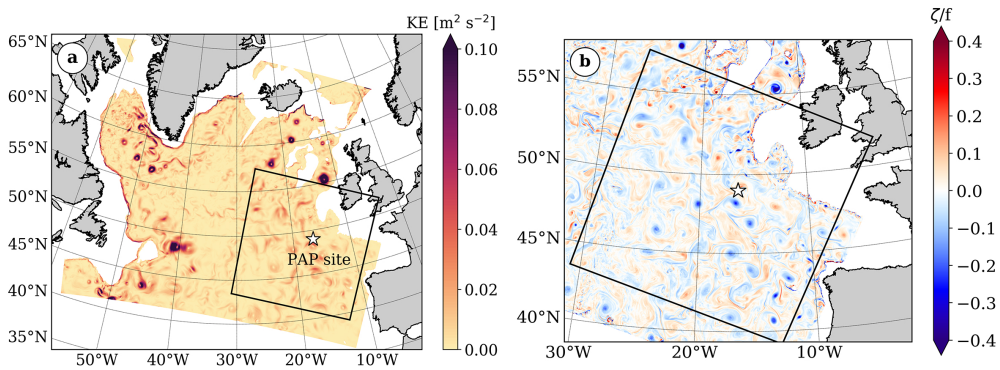
- 778 particle sinking, and the interpretation of sediment trap data. *Journal of Geophysical*
 779 *Research*, 95(C4), 5305.
- 780 Siegelman, L., Klein, P., Rivire, P., Thompson, A., Torres, H., Flexas, M., & Menemenlis, D.
 781 (2020). Enhanced upward heat transport at deep submesoscale ocean fronts. *Nature*
 782 *Geoscience*, 13(1), 50-55.
- 783 Stukel, M., Aluwihare, L., Barbeau, K., Chekalyuk, A., Goericke, R., Miller, A., ... Landry,
 784 M. (2017). Mesoscale ocean fronts enhance carbon export due to gravitational sinking
 785 and subduction. *Proceedings of the National Academy of Sciences*, 114(6), 1252-1257.
- 786 Taylor, J. R., Smith, K. M., & Vreugdenhil, C. A. (2020). The influence of submesoscales
 787 and vertical mixing on the export of sinking tracers in large-eddy simulations. *Journal*
 788 *of Physical Oceanography*, 50(5), 1319-1339.
- 789 Thomas, L. N., Tandon, A., & Mahadevan, A. (2008). Submesoscale processes and dynamics.
 790 In M. W. Hecht & H. Hasumi (Eds.), *Geophysical Monograph Series* (Vol. 177, p. 17-
 791 38). Washington, D. C.: American Geophysical Union.
- 792 Trull, T., Bray, S., Buesseler, K., Lamborg, C., Manganini, S., Moy, C., & Valdes, J.
 793 (2008). In situ measurement of mesopelagic particle sinking rates and the control
 794 of carbon transfer to the ocean interior during the vertical flux in the global ocean
 795 (vertigo) voyages in the north pacific. *Deep Sea Research Part II: Topical Studies in*
 796 *Oceanography*, 55(14-15), 1684-1695.
- 797 Turner, J. (2002). Zooplankton fecal pellets, marine snow and sinking phytoplankton
 798 blooms. *Aquatic Microbial Ecology*, 27, 57-102.
- 799 Turner, J. (2015). Zooplankton fecal pellets, marine snow, phytodetritus and the oceans
 800 biological pump. *Progress in Oceanography*, 130, 205-248.
- 801 Vic, C., Gula, J., Roullet, G., & Pradillon, F. (2018). Dispersion of deep-sea hydrothermal
 802 vent effluents and larvae by submesoscale and tidal currents. *Deep Sea Research Part*
 803 *I: Oceanographic Research Papers*, 133, 1-18.
- 804 Vic, C., Hascoët, S., Gula, J., Huck, T., & Maes, C. (2022). Oceanic Mesoscale Cy-
 805 clones Cluster Surface Lagrangian Material. *Geophysical Research Letters*, 49(4),
 806 e2021GL097488.
- 807 Villa-Alfageme, M., de Soto, F., Le Moigne, F. A. C., Giering, S. L. C., Sanders, R., &
 808 Garca-Tenorio, R. (2014). Observations and modeling of slow-sinking particles in the
 809 twilight zone. *Global Biogeochemical Cycles*, 28(11), 1327-1342.
- 810 Waite, A., Stemmann, L., L.and Guidi, Calil, P., Hogg, A., Feng, M., Thompson, P., ...
 811 Gorsky, G. (2016). The wineglass effect shapes particle export to the deep ocean in
 812 mesoscale eddies: The wineglass effect. *Geophysical Research Letters*, 43(18), 9791-
 813 9800.
- 814 Waniek, J., Koeve, W., & Prien, R. (2000). Trajectories of sinking particles and the
 815 catchment areas above sediment traps in the northeast atlantic. *Journal of Marine*
 816 *Research*, 58, 983-1006.
- 817 Wekerle, C., Krumpen, T., Dinter, T., von Appen, W.-J., Iversen, M., & Salter, I. (2018).
 818 Properties of sediment trap catchment areas in fram strait: Results from lagrangian
 819 modeling and remote sensing. *Frontiers in Marine Science*, 5, 407.
- 820 Yu, X., Naveira Garabato, A., Martin, A., Buckingham, C., Brannigan, L., & Su, Z. (2019).
 821 An annual cycle of submesoscale vertical flow and restratification in the upper ocean.
 822 *Journal of Physical Oceanography*, 49(6), 1439-1461.
- 823 Zhang, Z., Qiu, B., Klein, P., & Travis, S. (2019). The influence of geostrophic strain on
 824 oceanic ageostrophic motion and surface chlorophyll. *Nature Communications*, 10(1),
 825 2838.

Accepted Article

Table 1. Quantitative information for particle source regions. The left two columns list trap depths and particle sinking velocities. The right three columns are mean displacement (r_{mean}), the radial distance containing 95% of the source region ($R_{95\%}$), and the percentage of source area with PDF larger than $10^{-2}\%$, respectively.

Depth [m]	w_{sed} [m d ⁻¹]	r_{mean} [km]	$R_{95\%}$ [km]	$S_{PDF>10^{-2}\%}$ [%]
1000	20	190	394	41.6
1000	50	116	230	62.5
1000	100	76	146	72.8
1000	200	47	90	80.7
2000	20	236	490	31.4
2000	50	141	280	52.6
2000	100	96	194	66.1
2000	200	64	118	76.8

Accepted Article



826

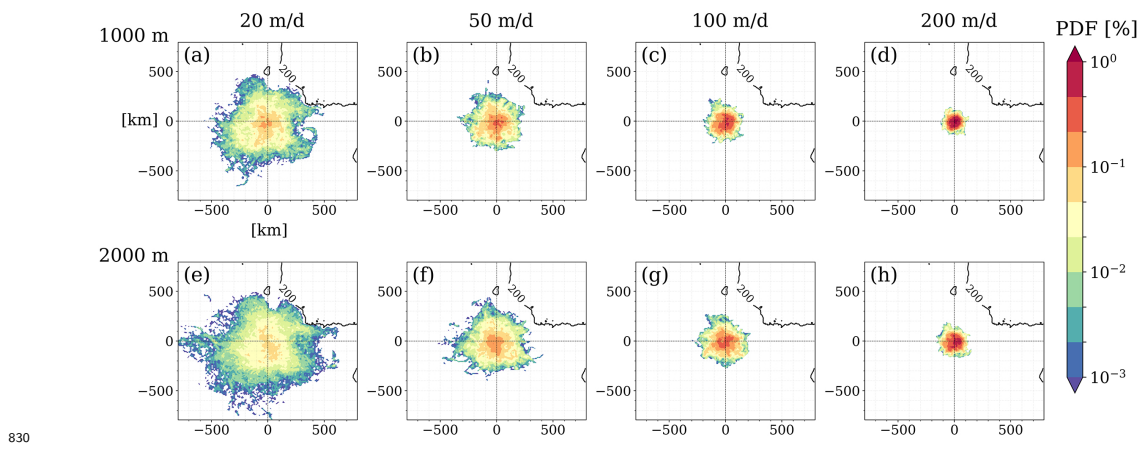
827

828

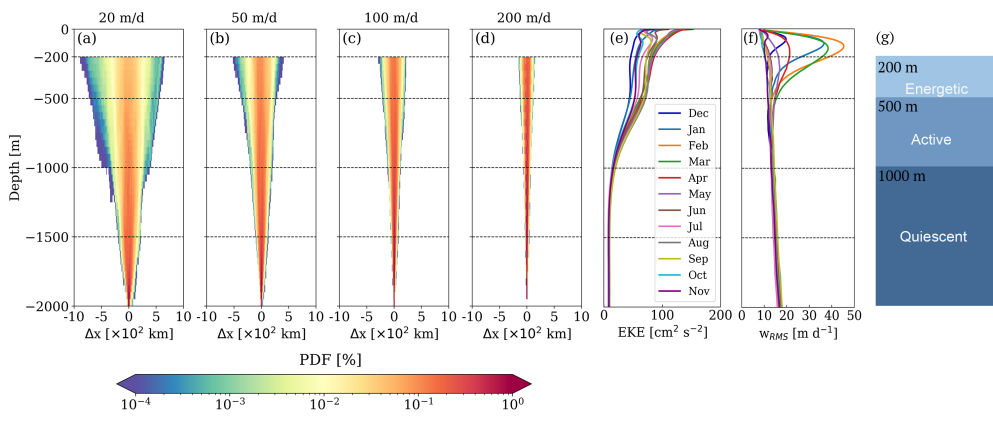
829

Figure 1. Snapshots of (a) kinetic energy at 1000 m for the whole POLGYR domain and (b) a zoomed relative vorticity field at 1000 m. The study region is in the black box centered on the PAP site (white star).

Accepted Article



831 **Figure 2.** Source region at 200 m for particles collected by the moored sediment traps over
 832 the seven years (2002 - 2008), with different sinking velocities from two trap depths (a-d, 1000 m;
 833 e-h, 2000 m). Particle positions are binned into a 10 km \times 10 km grid. The color indicates the
 834 percentage, i.e., the number of particles in each bin divided by the total amount of particles. The
 835 black contour is the 200 m isobath.



836

837

838

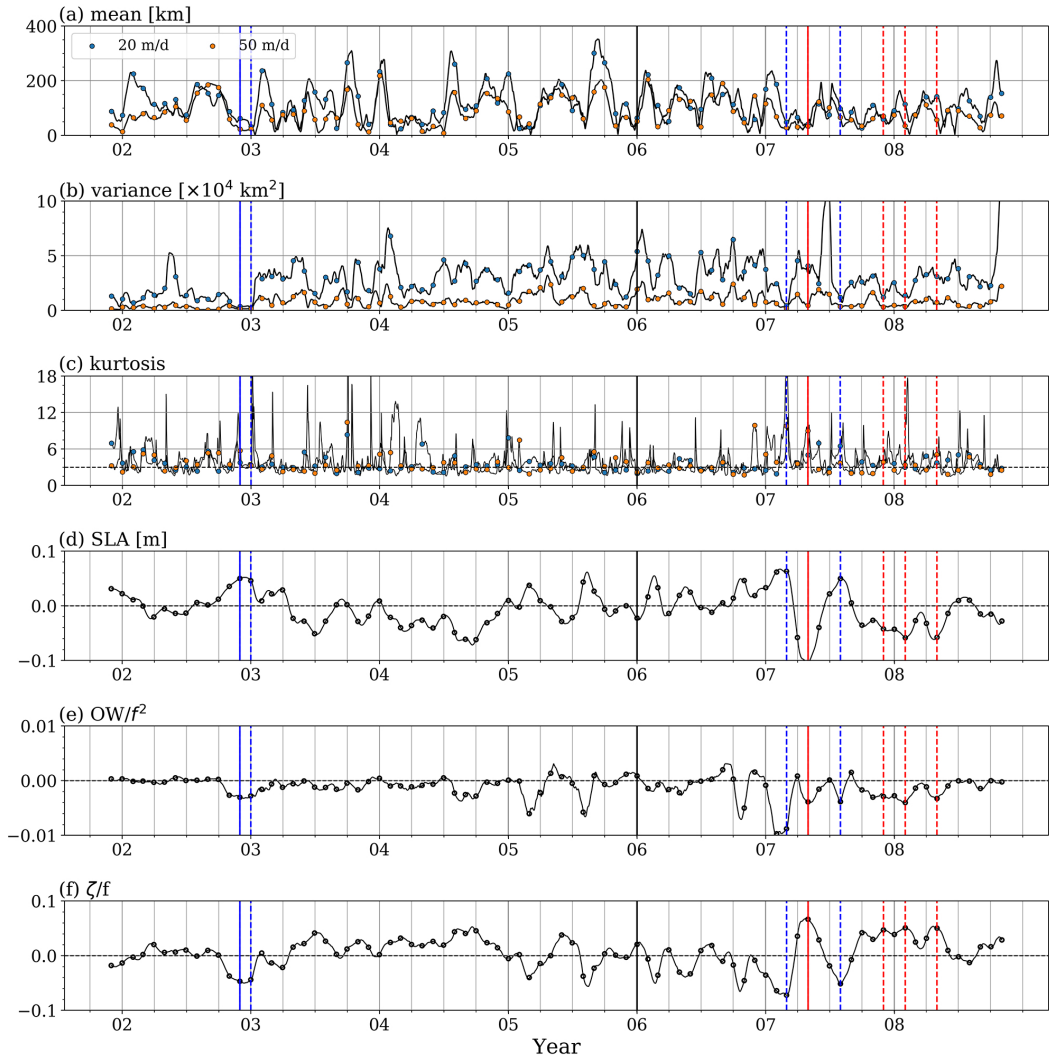
839

840

841

842

Figure 3. (a-d) Seven-year integrated particle trajectories backtracked from 2000 m, projected on the zonal section with a bin size of $10 \text{ km} \times 50 \text{ m}$. The color indicates the percentage, i.e., the number of particles in each bin divided by the total amount of particles. (e-f) Vertical profiles of monthly climatology eddy kinetic energy (EKE) and root-mean-square vertical velocity w_{rms} averaged over 200×200 km domain. (g) A conceptual diagram of the three-layer structure of the water column based on the change of dynamics.



843

844

845

846

847

848

849

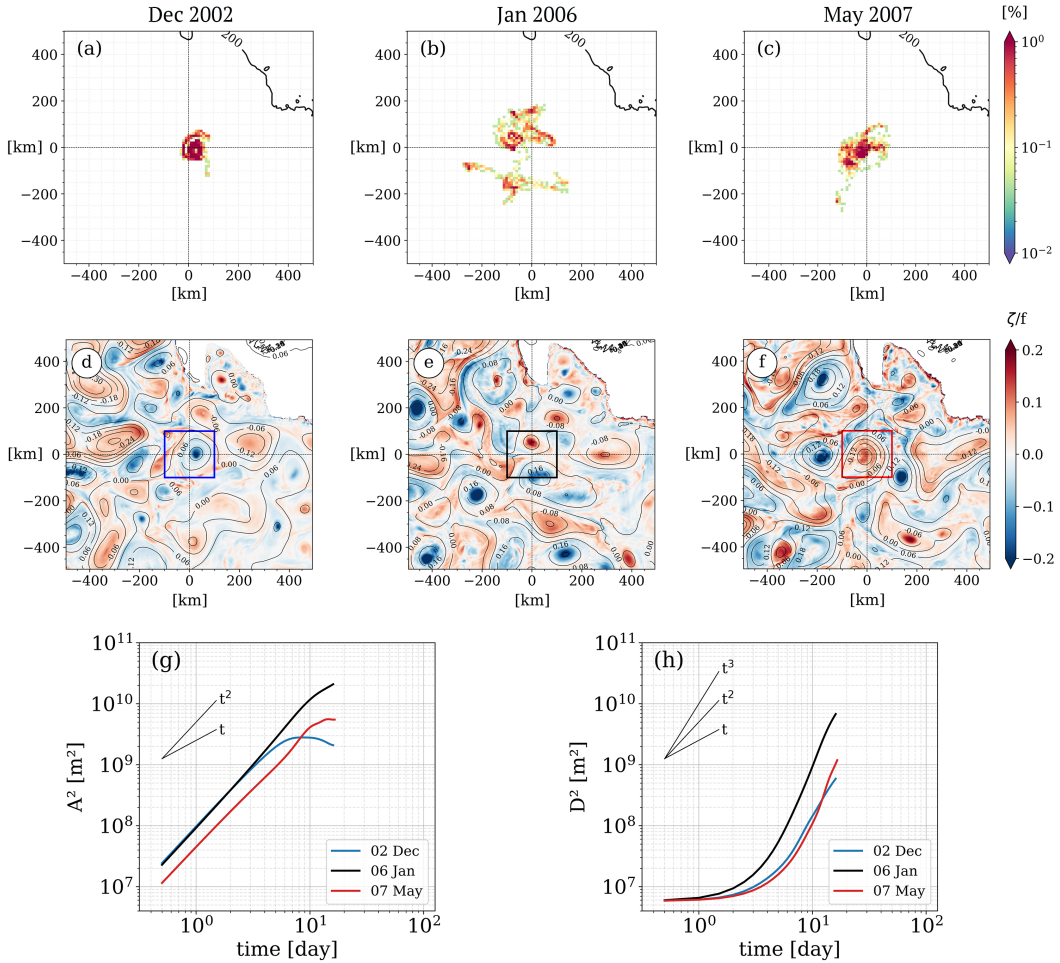
850

851

852

853

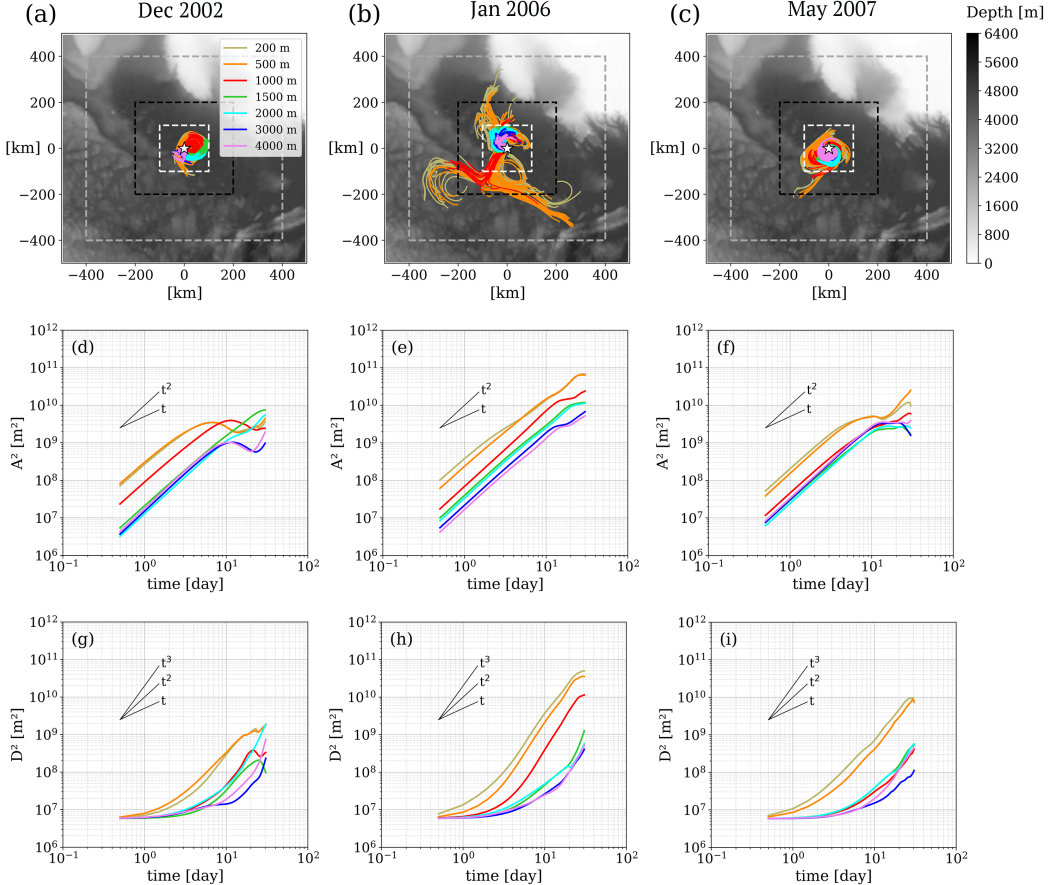
Figure 4. Time series of dispersion metrics derived from the probability density function (PDF) of particle horizontal displacements, for particles backtracked from 1000 m sinking at 50 m d^{-1} and 20 m d^{-1} : (a) mean; (b) variance; (c) kurtosis. (d-f) Monthly averaged sea level anomaly (SLA), Okubo-Weiss parameter normalized by f^2 and relative vorticity normalized by f in a $100 \times 100 \text{ km}$ square centered on PAP site. The vertical lines mark the typical months selected for further analysis: blue for the anticyclonic eddy dominated period, red for the cyclonic eddy dominated period, and black for the reference period (non-vorticity-dominated case). Solid lines highlight the main examples used in detailed analyses in Section 3.2, while the dashed lines mark alternative cases to firm the results presented in Section 3.4. The x-axes are labeled with ‘year’ at the beginning of each year.



854

855
856
857
858

Figure 5. (a-c) Probability density of particles sinking at 50 m d^{-1} to the 1000 m trap during three example periods. (d-f) Monthly averages of relative vorticity at 500 m with contours of sea level anomaly (SLA). (g-h) The group averaged absolute and relative dispersion. The “time” on the x-axis represents days after particles are released, i.e., particle “age”.



859

860

861

862

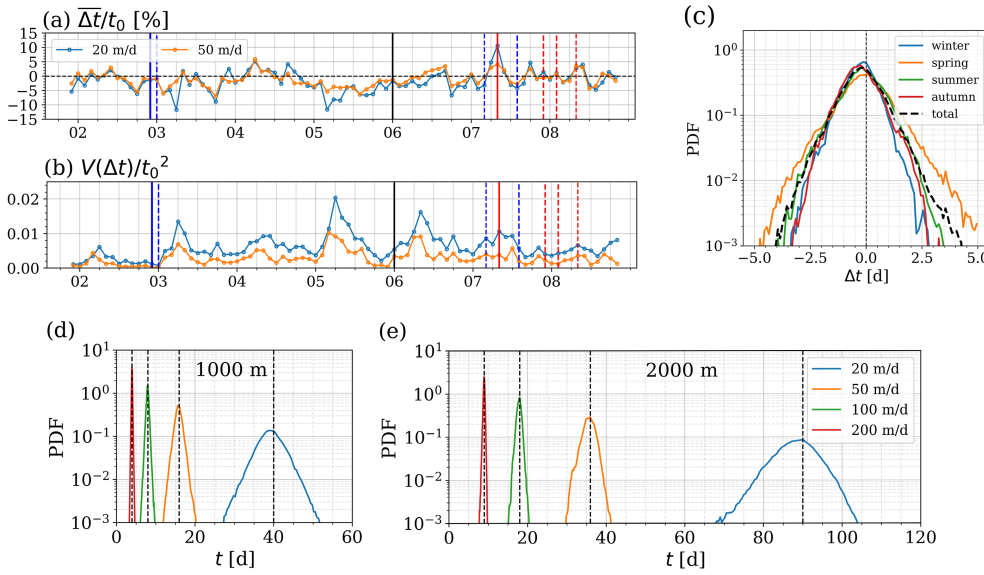
863

864

865

866

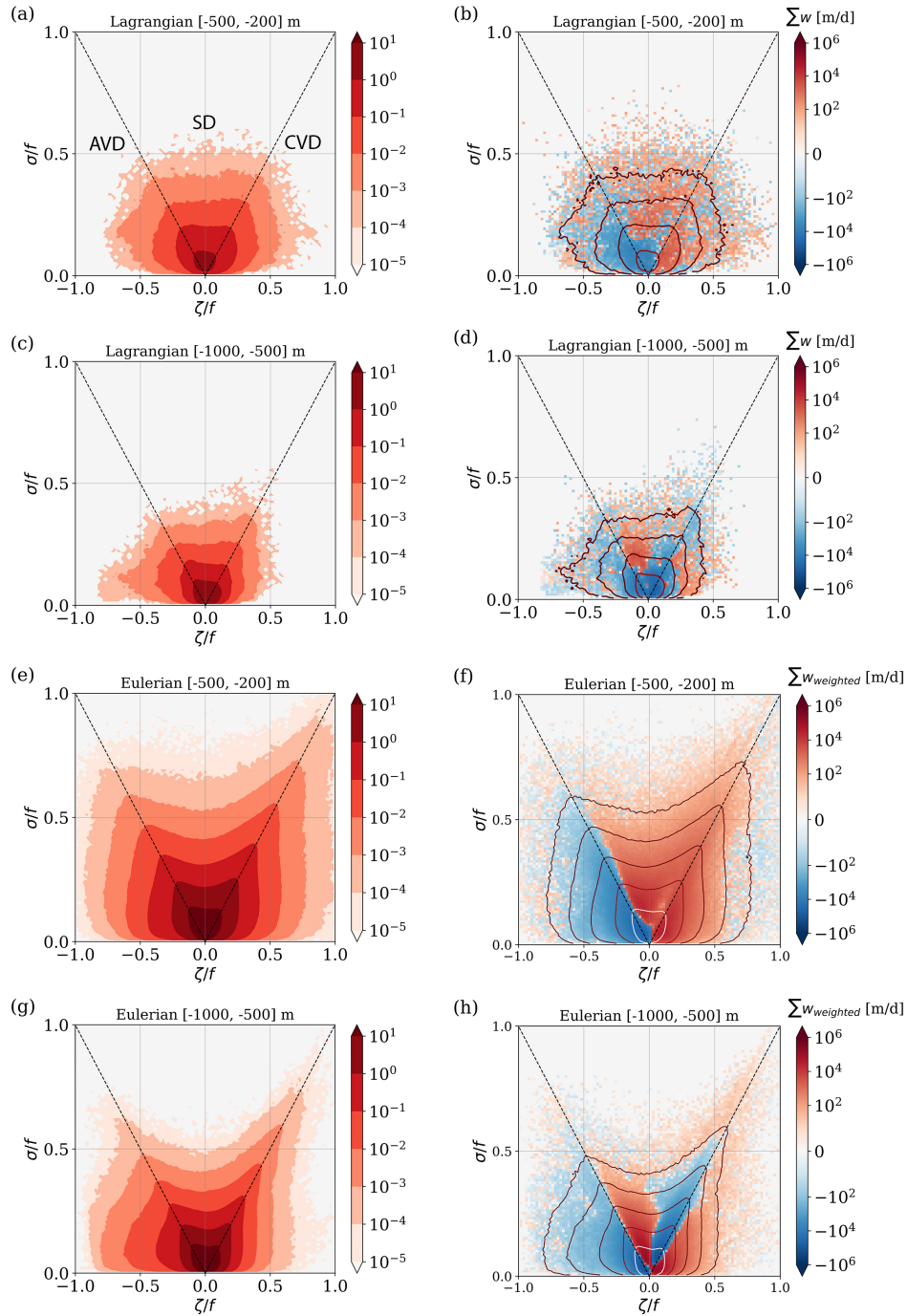
Figure 6. Trajectories and dispersion of particles in 2D simulations during the three example periods. (a-c) Trajectories of 200 particles randomly selected from 2160 particles backtracked at each depth in a month. The white star in the center represents the PAP site. The small white square (200×200 km) highlights the region with particles concentrated at all depths. The medium black square (400×400 km) covers most particle trajectories backtracked below 1000 m. The large grey square (800×800 km) contains all particle trajectories. The middle and bottom rows are (d-f) absolute dispersion and (g-i) relative dispersion as a function of release time.



867
868
869
870
871
872
873
874
875

Figure 7. Metrics of vertical dispersion for particles backtracked from 1000 m sinking at 50 m d^{-1} and 20 m d^{-1} : (a) The percentage of mean travel time anomaly (Δt) to the standard travel time t_0 ; (b) Variance of Δt normalized by t_0^2 . The colored vertical lines are the same as those in Figure 4, which marks months with local coherent anticyclonic eddy (in blue), cyclonic eddy (in red), and a reference case without coherent structure at the site (in black). (c) PDF of the travel time anomaly Δt for particles sinking at 50 $m d^{-1}$ backtracked from 1000 m depth, over full-period (7 years) and different seasons. (d-e) The PDF of travel time t over the seven-year full period for four sinking velocities and two trap depths.

Accepted Article



876

877

878

879

880

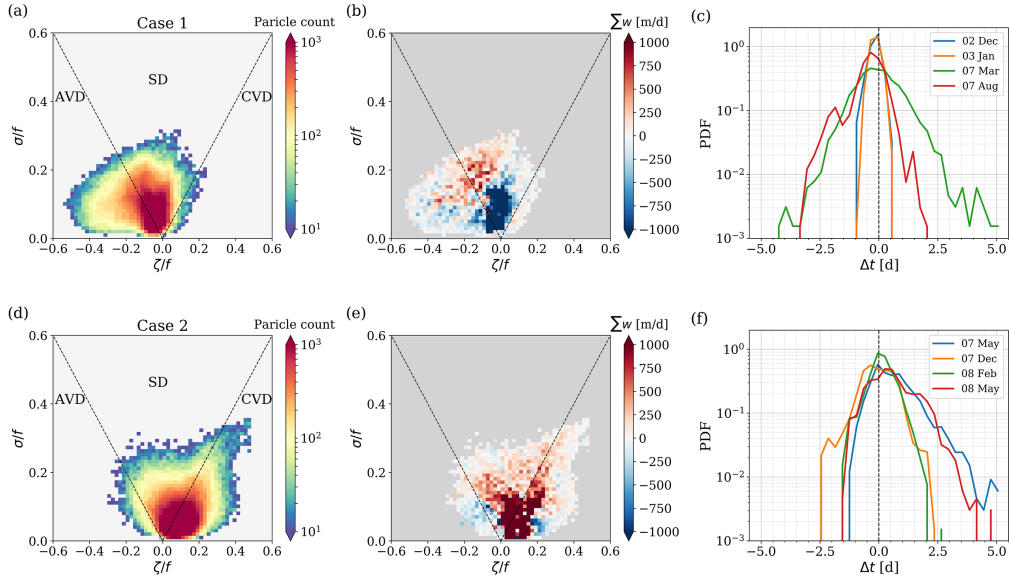
881

882

883

884

Figure 8. Comparison of Lagrangian trajectories (sinking velocity 50 m d^{-1}) and Eulerian field (domain size: $200 \times 200 \text{ km}$) on the vorticity-strain space. Left column: Joint Probability Density Function (JPDF). The x-y space is divided into three regions: anticyclonic vorticity dominated (AVD), cyclonic vorticity dominated (CVD), and strain dominated (SD). Right column: vertical velocity w conditioned on the vorticity-strain space, shown as the sum of w in each bin, contoured by the particle density. The sum of Eulerian w is weighted by the thickness of each depth layer in the sigma coordinate. (a-b) For particle footprints in 200-500 m. (c-d) For particle footprints in 500-1000 m. (e-f) For the Eulerian field in 200-500 m. (g-h) For the Eulerian field in 500-1000 m.

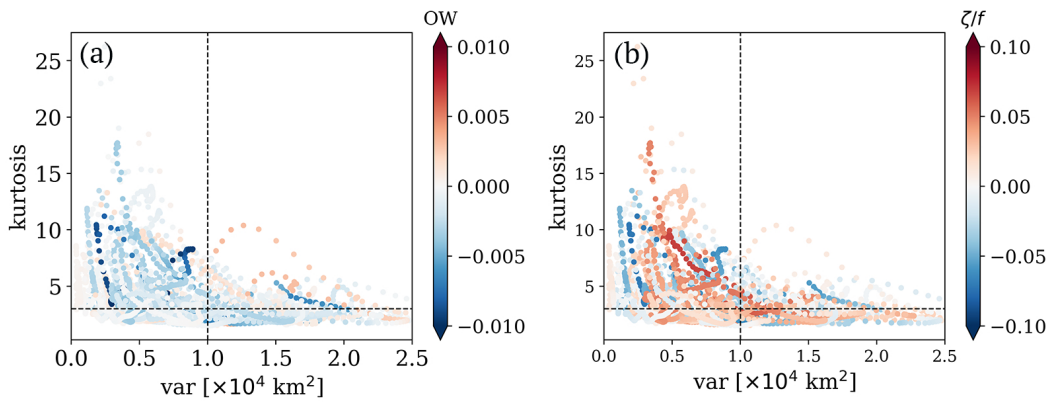


885

886
887
888
889

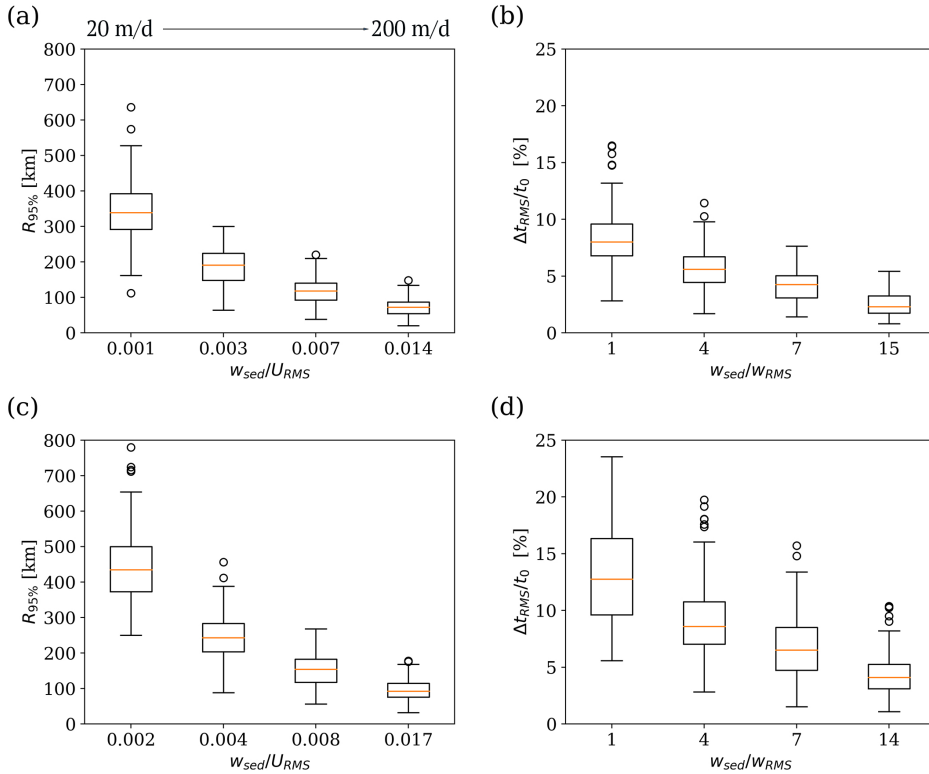
Figure 9. Composite plots of the eddy dominated periods: (a-c) Case 1: anticyclonic eddy-dominated periods; (d-f) Case 2: cyclonic eddy-dominated periods. From left to right columns are particle count on the vorticity-strain space, the conditioned sum w , and PDF of travel time

Accepted Article



890
891
892
893

Figure 10. Relation between kurtosis and variance from 30-day moving average time series for 50 m d^{-1} , trap 1000 m, colored by (a) Okubo-Weiss parameter and (b) relative vorticity. The dashed lines mark variance = $1 \times 10^4 \text{ km}^2$ and kurtosis = 3.



894
895
896
897
898
899
900
901

Figure 11. Full-period monthly horizontal and vertical dispersion metrics as a function of the ratio of sinking speed (from left to right: 20, 50, 100, 200 m day⁻¹) to the flow velocity. Top panel for particles backtracked from 1000 m: (a) The radial distance containing 95% of the source region ($R_{95\%}$), corresponding to the ratio of particle sinking velocity (w_{sed}) to the root-mean-squared (RMS) horizontal current velocity (U_{RMS}). (b) RMS travel time anomaly (Δt_{RMS}) normalized by standard travel time t_0 , corresponding to the ratio of particle sinking velocity to the RMS vertical flow velocity (w_{RMS}). Bottom panel (c-d): same as a-b, for particles backtracked from 2000 m.